The International Journal of Advanced Manufacturing Technology (2018) 96:963–972
https://doi.org/10.1007/s00170-018-1635-4

ORIGINAL ARTICLE

Investigation on flow field of ultrasonic-assisted abrasive waterjet using CFD with discrete phase model

Zhe Lv[1] · Rongguo Hou[1] · Yebing Tian[1] · Chuanzhen Huang[2] · Hongtao Zhu[2]

Received: 22 September 2017 / Accepted: 15 January 2018 / Published online: 3 February 2018

Abstract
The characteristics of flow field have significant influence on impact erosions of containing particles in abrasive waterjet machining. However, measurement of velocity and pressure distributions in flow field is hard to implement. In present study, computational fluid dynamics (CFD) is utilized to model the abrasive waterjet flow field in ultrasonic-assisted abrasive waterjet machining with the aid of discrete phase method. The workpiece vibration is simulated by using dynamic mesh method. The effect of ultrasonic vibration on pressure and velocity distributions was investigated, as well as the particle impact parameters such as local impact angle and velocity. The results indicate that the pressure value is lower when vibration is applied on target and the lateral flow along the vibration direction is enhanced and affected the high pressurized water film. Moreover, the particle velocity is higher when vibration is introduced due to the fact that the weakening of stagnation effect owing to the shear of vibrating target surface. In addition, ultrasonic-assisted abrasive waterjet erosion experiments were conducted to explore the practical effects on material removal and erosion mechanism. The experimental results verify that application of ultrasonic vibration is considered to facilitate the material removal of abrasive waterjet.

Keywords Computational fluid dynamics · Abrasive waterjet · Impact flow field · Ultrasonic vibration

1 Introduction

Erosion is a common natural phenomena mostly caused by wind, water, and sand. In industrial situations, erosive wear often occurs at oil pipeline and turbine due to the repeatedly corrosions of contamination particles. Inspired by that, abrasive particles are mixed with the high-velocity water to cut and etch various kinds of material [1, 2]. The abrasive waterjet machining has the advantage of low thermal effect and clean. With the application of high-accuracy motion control and finer injection nozzle, abrasive waterjet is used in precision machining and surface processing [3–5].

✉ Zhe Lv
lzjslyz@126.com

[1] School of Mechanical Engineering, Shandong University of Technology, Zibo 255000, China

[2] Center for Advanced Jet Engineering Technologies (CaJET), Key Laboratory of High-Efficiency and Clean Mechanical Manufacture (Ministry of Education), School of Mechanical Engineering, Shandong University, Jinan 250061, China

Zhu et al. [6] conducted the fine abrasive waterjet machining of ceramics and analyzed the stress field at the impact zone induced by the particle. The results indicated that the use of fine abrasives and low water pressure inhibits the fracture and facilitates the improvement of machining quality. Booij et al. [7] investigated the machining effect of glass by using abrasive slurry. Nanometer accurate shaping was achieved and mathematical model of machining spot was established. Pang et al. [8] studied the micro-channel formation mechanism in abrasive slurry jet machining of glass. The predictive model of material removal is also developed to optimize the process. Some researchers implemented computational fluid dynamics to investigate the characteristics of micro-abrasive waterjet machining. Mohammad et al. [9] used a low pressure abrasive slurry jet to machine micro-features such as holes and channels on glass. The effects of particle kinetic energy on channel erosion rate and bottom surface roughness were analyzed. A CFD model was established and implemented to calculate the local impact velocity and angle of particle. Kowsari et al. [10] utilized CFD to predict the erosion footprint in abrasive jet mirco-machining. The footprint size is influenced by both primary and secondary impacts. They also considered the effect of altering channel profile on the flow

field as well as the erosion rate [11]. Nouraei et al. [12] conducted the abrasive slurry jet machining of channels and used a CFD model to account for the actual impact velocities and angles of particles deflected by the streamline. The results indicated that the erosion due to slurry flow on side-walls can widen the channel.

Owing to the implementation of fine abrasives and low pressure, the material removal efficiency is relatively lower in abrasive waterjet precision machining [13–15]. Therefore, it is considered to combine abrasive waterjet with some other non-traditional machining method. Ultrasonic-assisted machining is extensively used to improve the efficiency of material processing. Uhlmann et al. [16] conducted the ultrasonic-assisted grinding of ceramics and found that the vibration of grinding wheel enhanced the tool engagement. The chip thickness was higher while the thermal loads were reduced due to the interrupted contact between grit and surface. Tian et al. [17] implemented the rotary ultrasonic milling of quartz glass and modeled the particle trajectory to analyze the interaction between ultrasonic hammering, spindle rotation, and feed rate. The experimental results implied that the high frequency dynamic impact action and larger nominal depth of cut due to ultrasonic vibration resulted in less surface fracture while higher surface roughness. Some researchers have used pulsating waterjet generated by the ultrasonic vibration converter to enhance the disintegration of biological materials. Zelenak et al. [18] found that the pressure necessary for the generation of pulsating jet is lower than continuous jet, and the impact pressure is considerably higher. Lehocka et al. [19] investigated the topography of cooper alloys created by pulsating water jet and found that the pulsation can enhance the squeezing of material at the cutting groove created by jet. Hreha et al. [18] studied the dependency of vibration emission frequency on abrasive flow rate. The measured vibration signals were used to analyze the surface topography evolution in cutting process. The present authors have conducted ultrasonic-assisted waterjet machining of aluminum nitride and found that the application of workpiece ultrasonic vibration can effectively enhance the material removal [20–22].

The characteristics of flow field have significant influence on impact erosions of containing particles. The motions and trajectories of abrasive particles are affected by the streamline at the impact zone of jet flow. However, measurement of variables in flow field is hard to implement. In the present study, CFD is utilized to model the abrasive waterjet flow field in ultrasonic-assisted abrasive waterjet machining with the aid of discrete phase method. The workpiece vibration is simulated by using dynamic mesh method. The effect of ultrasonic vibration on pressure and velocity distributions was investigated, as well as the particle impact parameters such as local impact angle and velocity. In addition, ultrasonic-assisted abrasive waterjet erosion experiments were conducted to explore the practical effects on material removal and erosion mechanism.

2 CFD modeling

2.1 Conservation equations

Eulerian multiphase flow is implemented to simulate the dynamic behaviors of waterjet surrounding by the air circumstance. The water and air phases are treated as interpenetrating continua, and the volume fractions are assumed to be continuous functions. The sum of volume fractions of both phases is unity. Coupling of different phases is through the inter-phase exchange of conservation equations. Continuity and motion equations for each phase are expressed as [6]:

$$\frac{\partial}{\partial}\left(\alpha_q\rho_q\right)+\nabla\cdot\left(\alpha_q\rho_q v_q\right)=\sum_{p=1}^{n}\left(m_{pq}-m_{qp}\right)+S_q \tag{1}$$

$$\frac{\partial}{\partial}\left(\alpha_q\rho_q v_q\right)+\nabla\cdot\left(\alpha_q\rho_q {v_q}^2\right) = -\alpha_q\nabla p+\nabla\cdot\tau_q+\alpha_q\rho_q g + \sum_{p=1}^{n}\left(R_{pq}+m_{pq}v_{pq}-m_{qp}v_{qp}\right)+F_q \tag{2}$$

where α_q is the volume fraction of phase q, ρ_q is the density, v_q is the velocity, m_{pq} is the mass transfer from the p_{th} to q_{th} phase, m_{qp} is the mass transfer from the q_{th} to p_{th} phase, S_q is the source term which is zero by default, τ_q is the stress-strain tensor of q_{th} phase, R_{pq} is interaction force between phases, and F_q is the external force.

The Reynold's number of fluid flow involved in AWJ is high and characterized by fully turbulence. The fluctuations of velocities and scalar quantities are described by k-ε turbulence model. The transportation equations of turbulence energy and dissipation rate shared by both phases can be expressed as [7]:

$$\frac{\partial}{\partial}(\rho k)+\nabla\cdot(\rho v k)=\nabla\cdot\left(\frac{\mu_t}{\sigma_k}\nabla k\right)+G_k-\rho\varepsilon \tag{3}$$

$$\frac{\partial}{\partial}(\rho\varepsilon)+\nabla\cdot(\rho v\varepsilon)=\nabla\cdot\left(\frac{\mu_t}{\sigma_\varepsilon}\nabla\varepsilon\right)+\frac{\varepsilon}{k}\left(C_{1\varepsilon}G_k-C_{2\varepsilon}\rho\varepsilon\right) \tag{4}$$

where $\rho=\sum_{i=1}^{N}\alpha_i\rho_i$, $v=\frac{\sum_{i=1}^{N}\alpha_i\rho_i v_i}{\sum_{i=1}^{N}\alpha_i\rho_i}$, μ_t is the turbulent viscosity, G_k is the production of turbulent kinetic energy, and $C_{1\varepsilon}$, $C_{2\varepsilon}$ are constants.

2.2 Discrete phase model

The volume fraction of abrasive particles dispersed in jet flow is low than 10% due to the low abrasive flow rate implemented in actual AWJ. Therefore, the solid particles are simulated as discrete phase entities in Lagrangian frame of reference rather than Eulerian treatment. The continuous fluid phase is solved by using time-averaged Navier-Stokes equations,

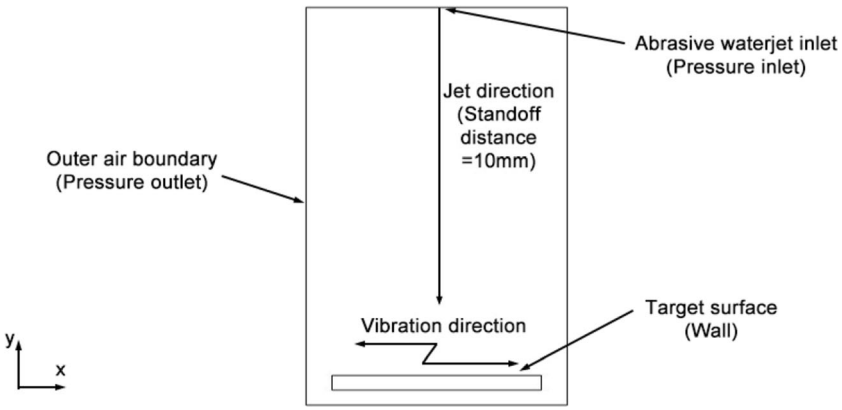

Fig. 1 Computational model of flow field

while the discrete phase is solved by tracking the dispersed particles through the computed flow field. The interactions between particles are neglected.

The motion equation of the discrete particle can be expressed as [9]:

$$\frac{du_p}{dt} = F_D(u-u_p) + \frac{g\left(\rho_p-\rho\right)}{\rho_p} + F_x \tag{5}$$

where u_p is the particle velocity, u is the fluid phase velocity, $F_D(u\text{-}u_p)$ is the drag force per unit particle mass, g is the gravity acceleration, ρ_p is the density of particle, ρ is the density of fluid, and F_x is the additional force due to inertia and pressure gradient of fluid. The trajectory of the particle can be calculated by integrating the force balance equation.

2.3 Boundary conditions

The geometry of computation domain is established using ANSYS FLUENT 14.5 and shown in Fig. 1. The nozzle is considered as a pressure inlet of water mixed with discrete particle phase. The diameter of the inlet is 0.76 mm and the pressure of inlet jet is ranged from 60 to 140 MPa, which correspond to the operation parameters in practical case. The silicon carbide particle streams are injected into the continuous fluid flow at the nozzle inlet as the discrete phase. The distribution of abrasive diameter is assumed to be uniform and ranged from 10 to 50 μm. The abrasive waterjet enters the domain filled full of air at the initialization. The outer boundary of the domain is set as the pressure outlet of immersing air and side flow with an atmosphere pressure.

The stand-off distance between nozzle to the surface of target is 10 mm. The surface is set as wall boundary condition. The normal and tangential reflection coefficients of discrete phase at the target surface were both set as 0.2 [23]. In ultrasonic-assisted abrasive waterjet machining, the workpiece is attached onto the end of ultrasonic horn and vibrates with it. Vibration direction is perpendicular with the jet impact velocity. The motion of the horn can be described by the kinematic differential equations. Under the harmonic

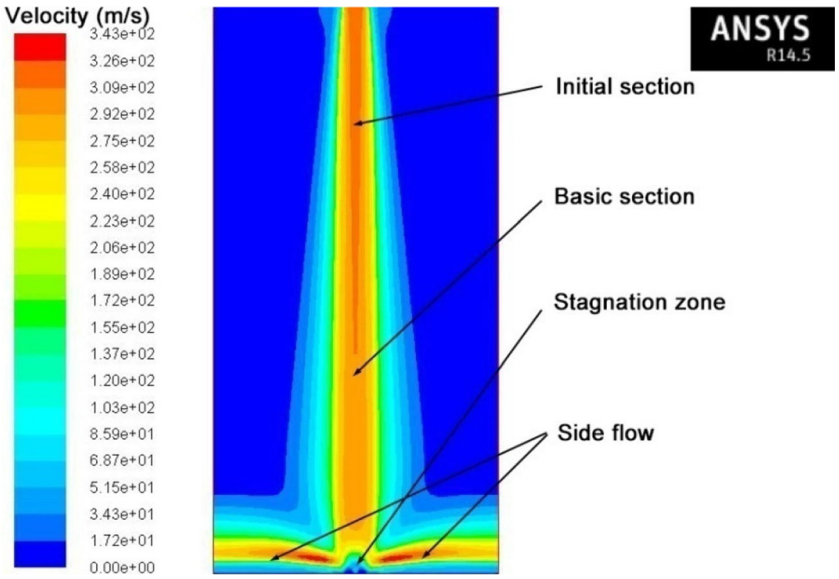

Fig. 2 Structure of impact jet flow (water pressure = 100 MPa)

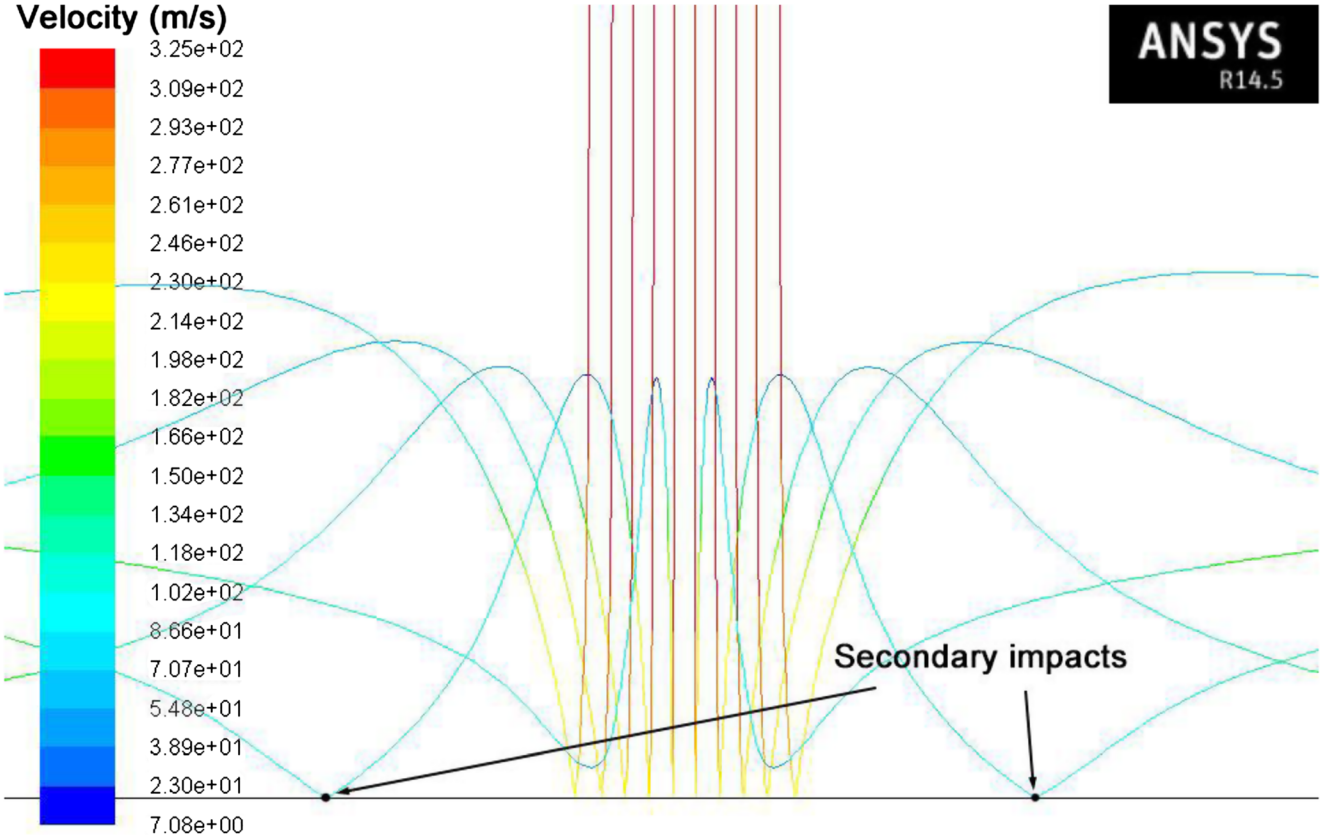

Fig. 3 Trajectories of particles in the impact flow field (water pressure = 100 MPa, abrasive diameter = 10 μm)

vibration condition, the vibrating velocity of the workpiece can be expressed as

$$v_f = 2\pi f A \cos 2\pi f t \tag{6}$$

where f is the vibration frequency and A is the vibration amplitude. In the actual processing, the ultrasonic frequency is 20 KHz and the amplitude is adjusted to 20 μm by changing the power input. Used defined function is compiled based on Eq. (6) with the define_grid_motion macro to control the motion of the target wall boundary. The associated mesh at the vicinity of vibrating wall is adapted by utilizing the layering dynamic meshing method. The relative motion of vibrating target and impinging jet is illustrated in Fig. 1.

The main part of computational domain is meshed with quadrilateral structural elements and the size is 0.05 mm × 0.05 mm. In order to insure the current mesh density has negligible effect on computational accuracy, a refined mesh with the size of was tested for comparison. The velocity results at the surface obtained by the refined mesh model only have a deviation of 3.4%. Therefore, it can be considered that the mesh density is acceptable for balancing accuracy and efficiency. Especially, the size of mesh adjacent to the target surface is improved as 0.025 mm × 0.025 mm considering the high gradients of flow field at wall boundaries.

3 Results and discussions

The basic structure of the jet fluid field is shown in Fig. 2. The upper region is free jet, which is comprised of initial and basic sections. The velocity of fluid at initial section maintains the same with the inlet velocity at the nozzle. The length of the initial section depends on turbulence and velocity distribution of fluid at the nozzle vicinity. As the jet travels downstream into the basic section, the mass and momentum exchange with the ambient air is

Table 1 Actual impact velocities and angles of particles at the target surface (water pressure = 100 MPa, abrasive diameter = 10 μm)

Particle no.	1	2	3	4	5	6	7	8	9	10
Impact velocity [m/s]	194	190	185	178	172	174	180	186	193	195
Impact angle [°]	67	73	79	82	85	87	81	78	73	67

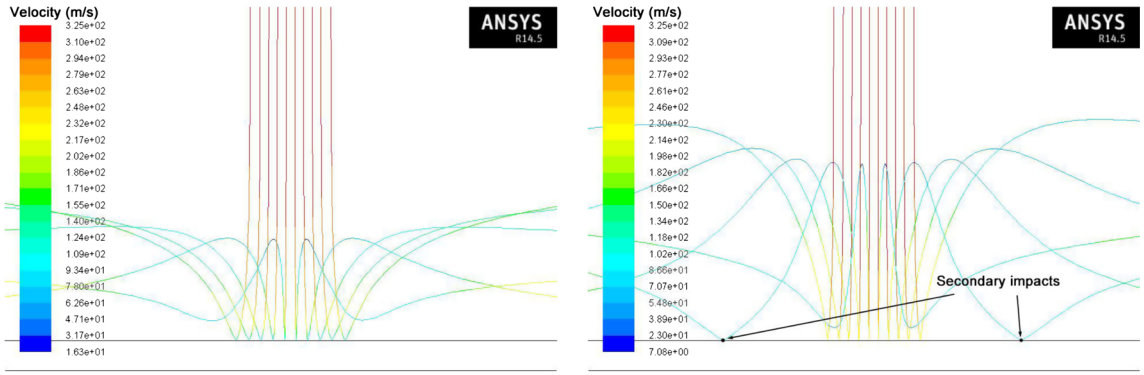

(a) 10μm (b) 50μm

Fig. 4 Trajectories of particles with different diameters (water pressure = 100 MPa)

intensified due to the gradient induced shear. The entrainment of surrounding air increases the diameter of jet and decays the velocity. Large amount of vortex arise at the interface and penetrate into the jet axis. Therefore, the basic section or main section is characterized by fully turbulence. When approaching the target surface, the jet turns into impact region. The axial velocity of jet fluid decreases significantly due to the resist of target surface and a local water film with high pressure is formed. Subsequent jet fluid is deflected by the stagnation and turn into side flow at peripheral region. The velocity of fluid field has a high gradient at the interface of stagnation and side flow region.

The motion of particle dispersed in water is mainly driven by the viscous drag force [24, 25]. At free jet zone, the velocity of particle is nearly equal to the surrounding water. When approaching the target surface, the stagnation zone intensively decreases the particle velocity. The particle tracks were obtained by using discrete phase model and shown in Fig. 3. Ten streams of particles were traced and numbered from left to right as 1 to 10. As illustrated in Table 1, the actual impact velocity of particle near the centerline of jet flow is 172 m/s rather than 325 m/s at the basic section of jet. Owing to the deflection of back flow at stagnation zone, the actual impact angle of abrasive particle deviates from the nominal jet impact angle.

Figure 4 shows the trajectories of impact particles with different abrasive diameter. The actual impact angles of particles are listed in Table 2. It can be found that the actual impact angles of particles with larger diameters are larger. The deviation of actual impact angle with jet impact angle is more obvious when small diameter particle is used. This is resulted from the fact that the smaller particle has stronger tendency to be deflected by the back flow caused by the stagnation zone. According to analysis of Humphrey [26], the tendency of particle to follow the streamline of carrying fluid can be characterized by the momentum equilibrium number λ:

$$\lambda = \frac{\rho_p (d_p)^2 v_j}{18 \mu d_n} \tag{7}$$

where ρ_d is the particle density, d_p is the particle diameter, v_j is the jet velocity, μ is the viscosity, and d_n is the nozzle diameter. A larger λ represents that the particle will unlikely follow the motion of fluid. Moreover, particles with larger diameter rebound to a higher position and tend to impact the surface for another time. The particles with smaller diameters near the centerline of the jet have more significant velocity decreases due to the decelerating of drag force. The decrease of impact angle and velocity will in turn affect the erosion capacity.

Figure 5 indicates the particle trajectories with different inlet pressure of jet. It can be found from Table 3 that the deviation of actual impact velocity and angle from that of jet

Table 2 Actual impact velocities and angles of particles with different diameters (water pressure = 100 MPa)

Particle no.	Abrasive diameter [μm]	Impact velocity [m/s]	Impact angle [°]
1	10	194	67
1	50	267	78
5	10	172	85
5	50	251	89

Table 3 Actual impact velocities and angles of particles with different water pressures (abrasive diameter = 10 μm)

Particle no.	Water pressure [MPa]	Impact velocity [m/s]	Impact angle [°]
1	60	146	57
1	140	232	71
5	60	124	80
5	140	220	87

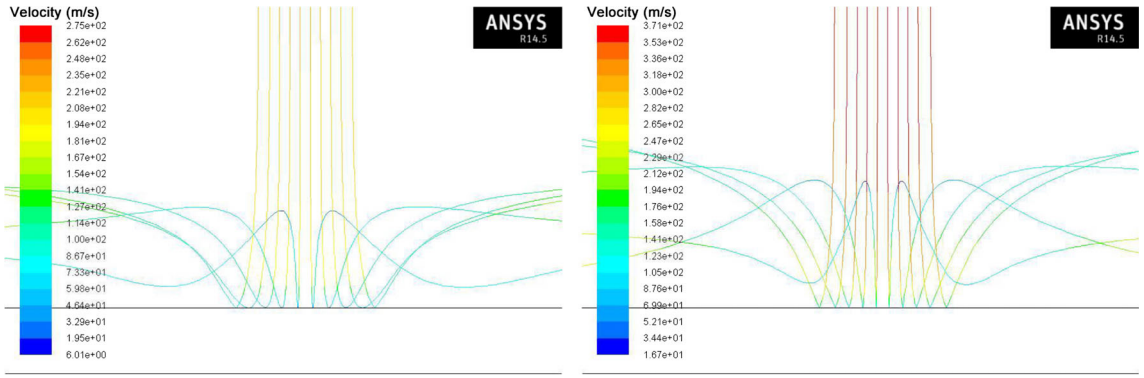

(a) Water pressure=60MPa (b) Water pressure=140MPa

Fig. 5 Particle tracks in flow field under different water pressure (abrasive diameter = 10 μm). **a** Water pressure = 60 MPa. **b** Water pressure = 140 MPa

flow is less at high water pressure. This can be also interpreted by the higher momentum equilibrium number at high jet velocity as Eq. (7) reveals.

Figure 6 reveals the pressure distribution of impact flow field at different moment of vibration period T. At the time $t = 0$ and $t = T/2$, the pressure value is lower than that at $t = T/4$. At $t = T/4$, the pressure (which has a maximum of 7.34 MPa) is approximately equal to that of non-vibration (which has a maximum of 7.32 MPa) as shown in Fig. 6a. Moreover, the shape of stagnation zone (where the pressure value is higher than 0.5 MPa) changes during the vibration period. According to Eq. (6), the velocity of the target is highest at $t = 0$, and turn to zero when $t = T/4$. This phenomenon indicates that the vibration of workpiece can reduce the stagnation effect due to the shear of the moving surface. The lateral flow along the vibration direction is enhanced and affected the high pressurized water film.

Figure 7 illustrates the particle trajectories at different time of vibrating period. It can be drawn from Table 4 that the particle velocity is higher at $t = 0$. This can be

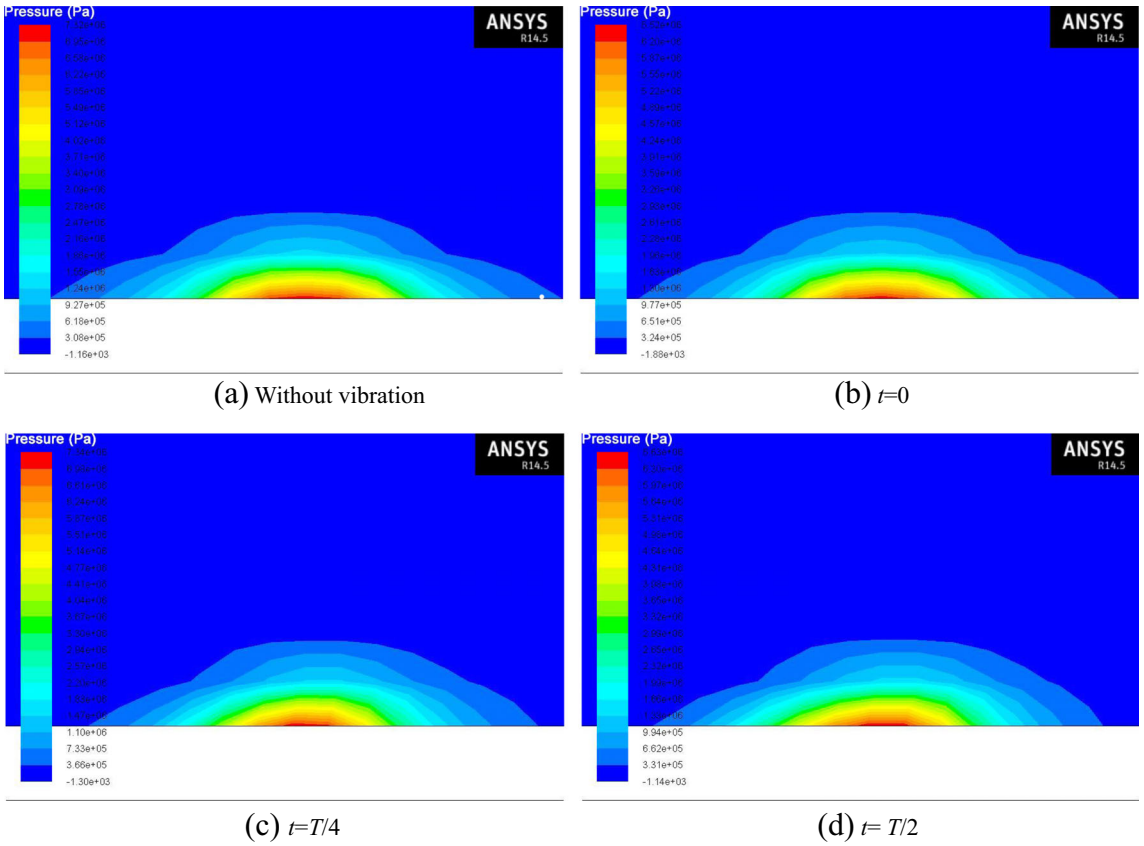

(a) Without vibration (b) t=0

(c) t=T/4 (d) t= T/2

Fig. 6 Pressure distribution in impact zone at different moment during a vibration period (water pressure = 100 MPa, abrasive diameter = 10 μm)

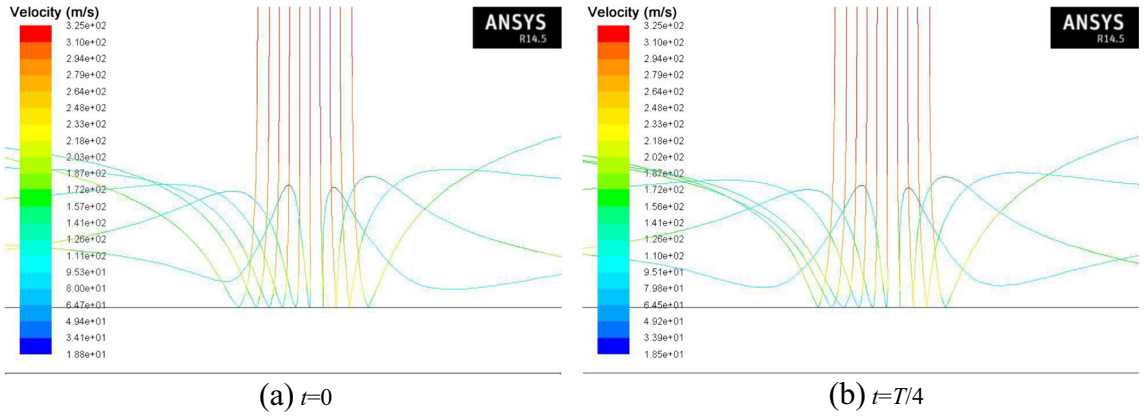

Fig. 7 Particle tracks at different time of vibration period (water pressure = 100 MPa, abrasive diameter = 10 μm)

attributed to the fact that the weakening of stagnation effect owing to the shear of vibrating target surface. The damping of particle kinetic energy by the drag force of back flow is decreased due to the vibration. In addition, the actual impact angle of particle is larger at $t = 0$ as a consequence of more slight deflection by the rebounded flow at stagnation zone.

According to [27], the erosion ability of particle is affected by the impact angle and velocity. For brittle materials, the dominant removal is resulted from initiation and coalescence of fractures. Larger impact velocity, especially the component vertical to the surface, contributes to the formation of lateral and radial cracks. Therefore, the results of fluid analysis indicate that the application of ultrasonic vibration is considered to facilitate the material removal of abrasive waterjet.

Table 4 Actual impact velocities and angles of particles at different time of vibration period (water pressure = 100 MPa, abrasive diameter = 10 μm, "N/A" means non-vibration)

Particle no.	Time of vibration period	Impact velocity [m/s]	Impact angle [°]
1	$t = 0$	207	72
1	$t = T/4$	198	68
1	N/A	194	67
5	$t = 0$	220	88
5	$t = T/4$	170	85
5	N/A	172	85

4 Experimental

4.1 Setup and conditions

Ultrasonic-assisted abrasive waterjet erosion experiments were conducted using a setup designed by the present authors [20]. The setup mainly consists of a waterjet apparatus and a ultrasonic vibration working stage as shown in Fig. 8. The pressurized water was generated by an intensifier and then conveyed to the jet nozzle. A robotic hand realized the motion of nozzle. The abrasive was added into the jet through a pneumatic feeder. Workpiece is fixed on the platform at the end of vibration stage. The vibration stage can transform electrical oscillation into mechanical vibration and actuate the movement of workpiece.

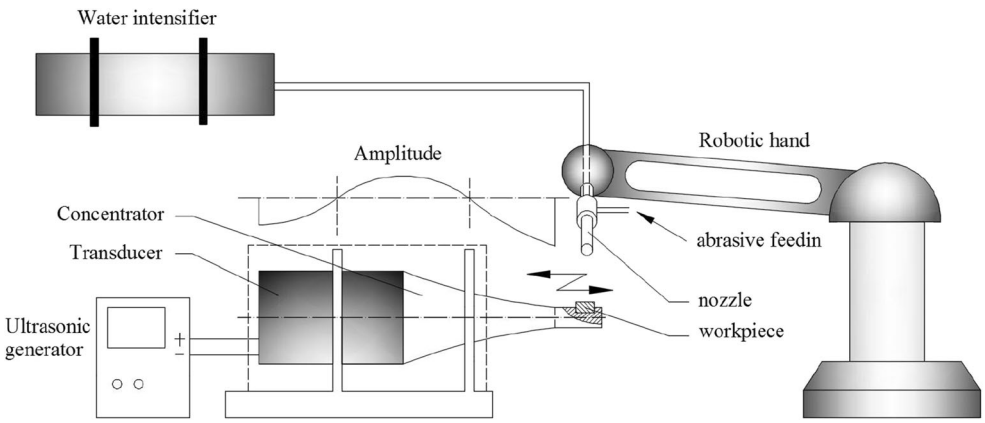

Fig. 8 Setup of ultrasonic-assisted waterjet erosion

Table 5 Properties of aluminum nitride

Properties	
Density [g/cm^3]	3.3
Vickers hardness [GPa]	12
Young modulus [GPa]	310
Flexural strength [MPa]	330
Fracture toughness [MPa·m$^{1/2}$]	3.2

Table 6 Properties of the silicon carbide

Material	Composition [%]		Density [g/cm^3]	Vickers hardness [GPa]
	SiC	Fe_2O_3		
SiC	> 97.5	< 0.7	3.2	31

Aluminum nitride specimen is used as the workpiece and silicon carbide particles are used as abrasives. The material properties of workpiece and abrasives are listed in Tables 5 and 6, respectively. Some experimental conditions are listed in Table 7. After every erosion trial, the surface was cleaned to remove the embedded abrasives. The eroded area is observed by implementing a laser scanning microscope. The material removal can be measured with the attached analysis module of microscope through integration of surface morphology data. For every parameter combination, three repeated trials were conducted to get the average value for reducing the scatter of experimental results.

4.2 Experimental results and discussions

The morphologies of workpiece surfaces eroded by abrasive waterjet with and without ultrasonic vibration are shown in Fig. 9. It is indicated that the eroded area with vibration is larger and the depth of the crater is higher. The erosion rate is calculated using the removal volume measured by the microscope:

Table 7 Experimental parameters

Parameters	
Vibration frequency [kHz]	20
Vibration amplitude [μm]	19.8
Vibration power output [W]	1600
Nozzle diameter [mm]	0.76
Water pressure [MPa]	60–140
Abrasive diameter [μm]	10–50
Impact angle [°]	90°
Stand-off distance [mm]	10
Abrasive feed rate [g/s]	0.2
Duration time of ejection [s]	2 s

$$Erosion\ \ rate = \frac{density\ \ of\ \ workpiece \times removal\ \ volume}{abrasive\ flow\ \ rate \times ejection\ \ time} \tag{8}$$

The erosion rates under different conditions are listed in Table 8. It can be found that the erosion rate increases with an increase of water pressure and abrasive diameter. This can be attributed to the higher kinetic energy transferred to abrasive particles when high pressure is adopted. Larger particles are more unlikely to be influenced by the drag force of viscous streamline at the stagnation zone. Therefore, the impact velocity and angle can retain a higher value to facilitate the material removal. Kowsari et al. [11] have drawn the similar findings in mirco-channeling of ceramics. Moreover, particles with larger

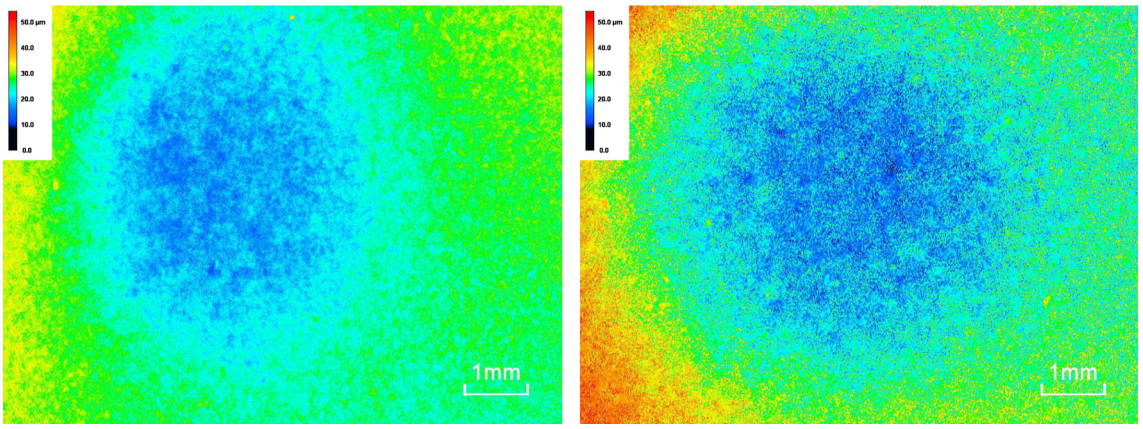

(a) Without vibration (b) With vibration

Fig. 9 The morphologies of erosion area created by abrasive waterjet with and without target vibration (water pressure = 100 MPa, abrasive diameter = 10 μm)

Table 8 Erosion rates under different experimental conditions

Parameter		Erosion rate with ultrasonic vibration [10 mg/g]	Erosion rate without ultrasonic vibration [10 mg/g]
Water pressure [MPa]	Abrasive diameter [μm]		
60	10	0.112	0.069
60	50	0.273	0.210
100	10	0.189	0.141
100	50	0.392	0.291
140	10	0.287	0.203
140	50	0.531	0.492

diameter are more likely to induce secondary impacts according to the simulation results in Section 4, which will in turn increase the material removal. Qi et al. [15] also found that the viscous flow induced erosion in ultrasonic vibration-assisted abrasive slurry jet machining of glass. Furthermore, the erosion rate is higher with the introduction of ultrasonic vibration. This is mainly owing to the higher actual impact velocity and angle as a consequence of the weakening of stagnation effect as discussed in Section 4.

5 Conclusions

CFD is utilized to model the abrasive waterjet flow field in ultrasonic-assisted abrasive waterjet machining with the aid of discrete phase model. The workpiece vibration is simulated by using dynamic mesh method. The simulation results indicated that the actual impact angles of particles with larger diameters are larger, whereas the smaller particle has stronger tendency to be deflected by the back flow caused by the stagnation zone. Moreover, particles with larger diameter rebound to a higher position and tend to impact for a second time. It is also found that the deviations of actual impact velocity and angle from that of jet flow are less at high water pressure. Furthermore, the pressure value is lower when vibration is applied on target, which indicates that the vibration of workpiece can reduce the stagnation effect due to the shear of the moving surface. The lateral flow along the vibration direction is enhanced and affected the high pressurized water film. The particle velocity is higher when vibration is introduced due to the fact that the weakening of stagnation effect owing to the shear of vibrating target surface. In addition, the actual impact angle of particle is larger as a consequence of more slight deflection by the rebounded flow at stagnation zone. Finally, ultrasonic-assisted abrasive waterjet erosion experiments were conducted. The results state that the erosion rate is higher with the introduction of ultrasonic vibration, which validates that the application of ultrasonic vibration is considered to facilitate the material removal of abrasive waterjet. The results of present investigation can provide some guidance for utilization and optimization of practical utilization. However, the current study is confined to the two-dimensional simulation, and in further study, three-dimensional model will be established. Moreover, the enhanced erosion induced by ultrasonic vibration of will be quantitatively calculated in future analyses.

Funding information This work is supported by the National Natural Science Foundation of China (51405274).

References

1. Hloch S, Valíček J (2012) Topographical anomaly on surfaces created by abrasive waterjet. Int J Adv Manuf Technol 59(5-8):593–604. https://doi.org/10.1007/s00170-011-3511-3
2. Liu D, Zhu H, Huang C, Wang J, Yao P (2016) Prediction model of depth of penetration for alumina ceramics turned by abrasive waterjet—finite element method and experimental study. Int J Adv Manuf Technol 87(9-12):2673–2682. https://doi.org/10.1007/s00170-016-8600-x
3. Alberdi A, Rivero A, López de Lacalle LN, Etxeberria I, Suárez A (2010) Effect of process parameter on the kerf geometry in abrasive water jet milling. Int J Adv Manuf Technol 51(5-8):467–480. https://doi.org/10.1007/s00170-010-2662-y
4. El-Domiaty AA, Abdel-Rahman AA (1997) Fracture mechanics-based model of abrasive waterjet cutting for brittle materials. Int J Adv Manuf Technol 13(3):172–181. https://doi.org/10.1007/BF01305869
5. Hou R, Huang C, Zhu H (2017) Experimental study on pulsation behavior of the ultrasonic vibration-assisted abrasive waterjet. Int J Adv Manuf Technol 91(9-12):3851–3859. https://doi.org/10.1007/s00170-017-0011-0
6. Zhu HT, Huang CZ, Wang J, Li QL, Che CL (2009) Experimental study on abrasive waterjet polishing for hard-brittle materials. Int J Mach Tools Manuf 49(7-8):569–578. https://doi.org/10.1016/j.ijmachtools.2009.02.005
7. Booij SM, van Brug H, Braat JJM, Fähnle OW (2002) Nanometer deep shaping with fluid jet polishing. Opt Eng 41(8):1926. https://doi.org/10.1117/1.1489677
8. Pang KL, Nguyen T, Fan JM, Wang J (2012) Modelling of the micro-channelling process on glasses using an abrasive slurry jet. Int J Mach Tools Manuf 53(1):118–126. https://doi.org/10.1016/j.ijmachtools.2011.10.005
9. Haj Mohammad Jafar R, Nouraei H, Emamifar M, Papini M, Spelt JK (2014) Erosion modeling in abrasive slurry jet micro-machining of brittle materials. J Manuf Process 17:127–140. https://doi.org/10.1016/j.jmapro.2014.08.006

10. Kowsari K, Nouhi A, Hadavi V, Spelt JK, Papini M (2017) Prediction of the erosive footprint in the abrasive jet micro-machining of flat and curved glass. Tribol Int 106:101–108. https://doi.org/10.1016/j.triboint.2016.10.038
11. Kowsari K, Nouraei H, Samareh B, Papini M, Spelt JK (2016) CFD-aided prediction of the shape of abrasive slurry jet micro-machined channels in sintered ceramics. Ceram Int 42(6):7030–7042. https://doi.org/10.1016/j.ceramint.2016.01.091
12. Nouraei H, Kowsari K, Samareh B, Spelt JK, Papini M (2016) Calibrated CFD erosion modeling of abrasive slurry jet micro-machining of channels in ductile materials. J Manuf Process 23:90–101. https://doi.org/10.1016/j.jmapro.2016.06.007
13. Qi H, Wen D, Yuan Q, Zhang L, Chen Z (2017) Numerical investigation on particle impact erosion in ultrasonic-assisted abrasive slurry jet micro-machining of glasses. Powder Technol 314:627–634. https://doi.org/10.1016/j.powtec.2016.08.057
14. Qi H, Xie Z, Hong T, Wang Y, Kong F, Wen D (2017) CFD modelling of a novel hydrodynamic suspension polishing process for ultra-smooth surface with low residual stress. Powder Technol 317:320–328. https://doi.org/10.1016/j.powtec.2017.05.030
15. Qi H, Wen D, Lu C, Li G (2016) Numerical and experimental study on ultrasonic vibration-assisted micro-channelling of glasses using an abrasive slurry jet. Int J Mech Sci 110:94–107. https://doi.org/10.1016/j.ijmecsci.2016.03.013
16. Uhlmann E, Spur G (1998) Surface formation in creep feed grinding of advanced ceramics with and without ultrasonic assistance. CIRP Ann Manuf Technol 47(1):249–252. https://doi.org/10.1016/S0007-8506(07)62828-5
17. Tian C, Chen X, Li D, Zhang W, Guan S (2017) Analysis of surface formation of rotary ultrasonic milling of quartz glass based on nano-indentation experiment. Procedia Eng 174:470–476. https://doi.org/10.1016/j.proeng.2017.01.168
18. Hreha P, Radvanská A, Hloch S, Peržel V, Królczyk G, Monková K (2015) Determination of vibration frequency depending on abrasive mass flow rate during abrasive water jet cutting. Int J Adv Manuf Technol 77(1-4):763–774. https://doi.org/10.1007/s00170-014-6497-9
19. Lehocka D, Klich J, Foldyna J, Hloch S, Krolczyk JB, Carach J, Krolczyk GM (2016) Copper alloys disintegration using pulsating water jet. Meas J Int Meas Confed 82:375–383. https://doi.org/10.1016/j.measurement.2016.01.014
20. Lv Z, Huang C, Zhu H, Wang J, Wang Y, Yao P (2015) A research on ultrasonic-assisted abrasive waterjet polishing of hard-brittle materials. Int J Adv Manuf Technol 78(5-8):1361–1369. https://doi.org/10.1007/s00170-014-6528-6
21. Lv Z, Huang C, Zhu H, Wang J, Yao P, Liu Z (2015) FEM analysis on the abrasive erosion process in ultrasonic-assisted abrasive waterjet machining. Int J Adv Manuf Technol 78:1641–1649. https://doi.org/10.1007/s00170-014-6768-5
22. Lv Z, Huang CZ, Wang J, Zhu HT, Che CL (2012) A 3D simulation on fluid field at the impact zone of abrasive water jet under different impact angles. Adv Mater Res 565:345–350. https://doi.org/10.4028/www.scientific.net/AMR.565.345
23. Kowsari K, Nouraei H, James DF, Spelt JK, Papini M (2014) Abrasive slurry jet micro-machining of holes in brittle and ductile materials. J Mater Process Technol 214(9):1909–1920. https://doi.org/10.1016/j.jmatprotec.2014.04.008
24. Li HZ, Wang J, Fan JM (2009) Analysis and modelling of particle velocities in micro-abrasive air jet. Int J Mach Tools Manuf 49(11):850–858. https://doi.org/10.1016/j.ijmachtools.2009.05.012
25. Li HZ, Lee A, Fan J, Yeoh GH, Wang J (2014) On DEM-CFD study of the dynamic characteristics of high speed micro-abrasive air jet. Powder Technol 267:161–179. https://doi.org/10.1016/j.powtec.2014.07.018
26. Humphrey JAC (1990) Fundamentals of fluid motion in erosion by solid particle impact. Int J Heat Fluid Flow 11(3):170–195. https://doi.org/10.1016/0142-727X(90)90036-B
27. Marshall DB, Lawn BR, Evans AG (1982) Elastic/plastic indentation damage in ceramics: the lateral crack system. J Am Ceram Soc 65(11):561–566. https://doi.org/10.1111/j.1151-2916.1982.tb10782.x